Eur. Phys. J. Plus (2026) 141:162
https://doi.org/10.1140/epjp/s13360-026-07303-6

THE EUROPEAN
PHYSICAL JOURNAL PLUS

Regular Article

Multi-technique characterizations of single-event burnout (SEB) in silicon carbide (SiC) power MOSFETs

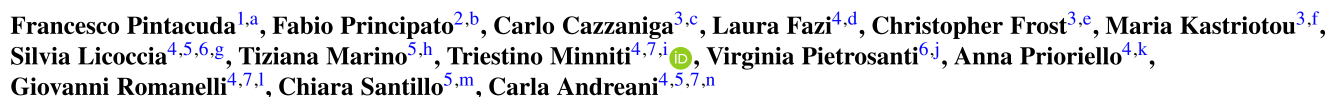

Francesco Pintacuda[1,a], **Fabio Principato**[2,b], **Carlo Cazzaniga**[3,c], **Laura Fazi**[4,d], **Christopher Frost**[3,e], **Maria Kastriotou**[3,f], **Silvia Licoccia**[4,5,6,g], **Tiziana Marino**[5,h], **Triestino Minniti**[4,7,i], **Virginia Pietrosanti**[6,j], **Anna Prioriello**[4,k], **Giovanni Romanelli**[4,7,l], **Chiara Santillo**[5,m], **Carla Andreani**[4,5,7,n]

[1] STMicroelectronics, Stradale Primosole 50, 95121 Catania, Italy
[2] Department of Physics and Chemistry Emilio Segrè-University of Palermo, viale delle scienze, Ed. 18, 90128 Palermo, Italy
[3] ISIS Facility, STFC, Rutherford Appleton Laboratory, Harwell OX11 0QX, United Kingdom of Great Britain and Northern Ireland
[4] NAST Centre c/o Physics Department, University of Rome Tor Vergata, Via della Ricerca Scientifica, 1, 00133 Rome, Italy
[5] Institute of Polymers, Composites and Biomaterials, National Council of Research, P.le E. Fermi, 1, 80155 Portici (NA), Italy
[6] Department of Chemical Sciences and Technologies, University of Rome Tor Vergata, Via della Ricerca Scientifica, 1, 00133 Rome, Italy
[7] Department of Physics, University of Rome Tor Vergata, Via della Ricerca Scientifica, 1, 00133 Rome, Italy

Received: 5 August 2025 / Accepted: 8 January 2026
© The Author(s) 2026

Abstract This study presents a comprehensive investigation of single-event burnout (SEB) in silicon carbide (SiC) power MOSFET employing multilevel advanced techniques. Firstly, the SEB was created by atmospheric neutron irradiation using the ChipIr beamline at ISIS Neutron and Muon Source Facility; to follow, the SEB was analyzed using the medium-range facilities X-Ray computed tomography (XCT), profilometry, and scanning electron microscopy (SEM), instrumentation suite of the ISIS@MACH ITALIA Facility (IM@IT). The use of complementary techniques—electrons, light, and neutron probes—provides new results that improve the knowledge of the SEB failure mechanism of SiC power MOSFET. By combining the results from such complementary techniques, this study allows to fully characterize the neutron-induced SEB, the 2D–3D morphology of the samples, and to evaluate the impact on the device. Neutron irradiation leads to a failure mechanism caused by the rapid heating that reaches the sublimation temperature of SiC leading to the displacement of the polyimide passivation layer, due to expansion stress, yielding consistent results of SEB maximum dimensions of $30 \times 30 \times 12\ \mu m$ and volume of about $9600\ \mu m^3$. These studies provide a 2D and 3D characterization of the SiC power MOSFET devices while reinforcing the need for radiation hardening strategies tailored to SiC-based power electronics for high-reliability applications such as automotive, aerospace, and nuclear energy.

1 Introduction

Radiation in the Earth's atmosphere originates from a combination of cosmic, solar, and terrestrial sources, with cosmic rays playing a dominant role in generating secondary radiation at high altitudes. Primary cosmic rays, mainly composed of high-energy protons and heavier nuclei from galactic and extragalactic sources, interact with atmospheric nuclei upon entering the Earth's atmosphere. These interactions lead to a cascade of secondary radiation, a process known as an extensive air shower, which produces a variety

[a] e-mail: francesco.pintacuda@st.com
[b] e-mail: fabio.principato@unipa.it
[c] e-mail: carlo.cazzaniga@stfc.ac.uk
[d] e-mail: laura.fazi@uniroma2.it
[e] e-mail: christopher.frost@stfc.ac.uk
[f] e-mail: maria.kastriotou@stfc.ac.uk
[g] e-mail: licoccia@uniroma2.it
[h] e-mail: tiziana.marino@cnr.it
[i] e-mail: triestino.minniti@uniroma2.it (corresponding author)
[j] e-mail: virginia.pietrosanti@uniroma2.it
[k] e-mail: anna.prioriello@uniroma2.it
[l] e-mail: giovanni.romanelli@uniroma2.it
[m] e-mail: chiara.santillo@cnr.it
[n] e-mail: carla.andreani@uniroma2.it

of secondary particles, including muons, pions, electrons, positrons, gamma rays, and neutrons [1]. Among these, neutrons (often called atmospheric neutrons) play a particularly significant role in the failure of power electronic devices, making them a critical factor in radiation exposure for aviation, space travel, and terrestrial environments [2]. Atmospheric neutrons are primarily produced in nuclear spallation reactions when high-energy primary cosmic rays collide with atmospheric nuclei, predominantly nitrogen and oxygen. These interactions produce secondary particles, including charged pions (π^+ and π^-) and neutral pions (π^0). While charged pions decay into muons and neutrinos, neutral pions rapidly decay into gamma rays, which can further contribute to electromagnetic cascades [3]. Additionally, nuclear fragmentation reactions release high-energy neutrons, which can travel significant distances before interacting with other atmospheric components. Neutron production is highly dependent on altitude and latitude due to variations in atmospheric density and to the influence of the Earth's geomagnetic field. At ground level (New York City), neutron flux results in 20 n cm^{-2} h^{-1} [4], 300 times lower of the one at 12 km [5]. Unlike charged secondary particles, such as muons, which experience magnetic deflection, neutrons remain unaffected by the Earth's magnetic field and can penetrate deeply into aircraft fuselages and spacecraft structures, increasing radiation exposure [6]. Failure of electronic devices due to terrestrial secondary radiation requires a significant deposition of charge in the semiconductor substrate of several fC/μm, in terms of the familiar notion of linear energy transfer (LET). It is not possible to obtain this amount of ionization by stopping of electrons, muons or photons, or even by stopping of protons or pions in the semiconductor via the electromagnetic interaction [7, 8]. A nuclear reaction is required to produce this amount of charge. As neutrons are the most penetrating radiation into the atmosphere, the most likely reaction will be a neutron–nucleus collision that gives rise to spallation fragments within or near the semiconductor substrate of a device. Still, more exotic ways of localized charge generation do exist, such as muon capture or pion reactions [9]. For that reason, atmospheric neutrons are a major source of single-event effects (SEEs) in microelectronics, particularly in avionics and satellite systems [9, 10]. SEEs are classified into soft errors, which are recoverable (e.g. single-event upset, SEU), and hard errors, which cause permanent failure (e.g. single-event latch-up, SEL, and single-event burnout, SEB) [11–17].

SiC-based power metal–oxide–semiconductor field-effect transistors (MOSFETs) are currently used in power systems in terrestrial applications, such as renewable energy systems, electric vehicles and their charging infrastructures, and train traction [18, 19]. The use of SiC is increasingly becoming attractive for power applications both in avionic and at ground level thanks to its excellent properties, such as higher breakdown field and thermal conductivity. Moreover, nuclear reactions at the base of the mentioned effects are expected to cause stress on the crystal structure of the devices, leading to changes in the electronic properties.

These devices are also suited to space electronic applications [20]. Among the several failure and degradation mechanisms that impact their reliability are the atmospheric neutron [20, 21]. The neutrons spectrum covers over twelve decades of neutron energy and the neutron flux increases with altitude, neutrons interaction with sensitive region of the power MOSFET may cause destructive events. The most common failure mechanism is the SEB which occurs when neutron–lattice collisions produce recoil atoms or spallation products that generate electron–hole pairs. This charge-plasma may turn on the parasitic bipolar junction transistor, which leads to excessive lattice temperature with consequent local lattice sublimation [22, 23]. SEB event primarily affects high-voltage power devices, such as MOSFETs and insulated-gate bipolar transistors (IGBTs). A SEB occurs when an energetic neutron or ion strike induces localized charge accumulation, triggering an avalanche breakdown in the drain-source or collector-emitter junction. This process leads to an uncontrolled surge in current, ultimately resulting in thermal runaway and irreversible device damage [13].

The risk of SEB is significantly heightened when a device operates near its maximum rated voltage, where the electric-field intensity is highest, increasing the charge carrier multiplication which can lead to the breakdown of the device. As power electronics continue to be widely implemented in space systems, avionics, and terrestrial applications exposed to high-energy radiation, mitigating SEBs is crucial for ensuring the reliability and longevity of electronic components. Neutron-induced SEB damage in SiC power MOSFETs exhibits similarities to the damage observed in SiC power diodes with equivalent voltage ratings [18]. Experimental studies on neutron-induced SEBs in high-voltage SiC MOSFETs revealed the formation of cracks on the device surface [18–20]. SEB-induced damage has been observed as localized thermal failure, primarily caused by current-induced avalanche events, while the emergence of surface cracks has been attributed to the expansion stress resulting from the sublimation of SiC [18].

In this study to test the neutron hardness of power MOSFETs, we performed accelerated neutron tests using neutron beams, with atmospheric-like neutron spectrum, at the ChipIr beamline at the ISIS Neutron and Muon Source, Rutherford Appleton Laboratory, U.K. [24, 25]. The main aim of the accelerated neutron tests was to estimate the failure in time (FIT) of the power devices (FIT corresponding to a failure in 10^9 device-hours) under different operating conditions (e.g. voltage bias, temperature) [12, 24–26]. Working at high-voltage conditions, the effect of ionizing radiation on operating SiC devices can bring to permanent damage through SEBs and SEEs, which contribute to the FIT rate. Further, we performed a morphological characterization of neutron-induced SEBs in SiC power MOSFETs using complementary analytical techniques, for a cross-comparison of experimental results to verify their consistency. The aim is to derive information of the 2D-3D morphology of the MOSFET, the atomic structure, the potential crystallographic burnout induced by the fast neutron irradiation and a materials-to-circuits characterizations with MRF analytical instrument to investigate the degree of damage by neutron-induced SEBs micro-burnings on SiC, occurred after accelerated neutron tests.

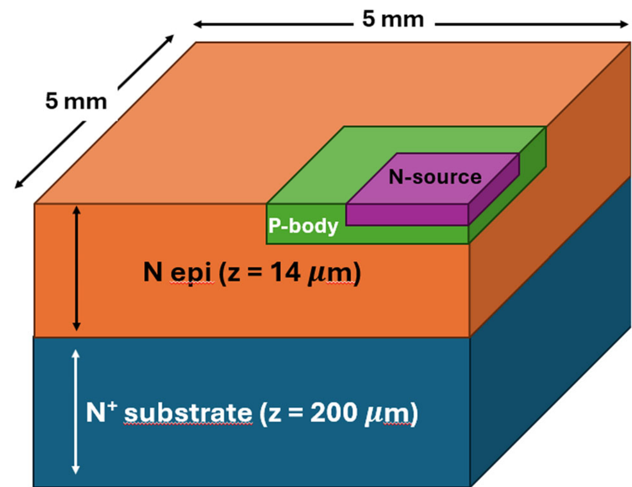

Fig. 1 Schematic of the power MOSFET structure

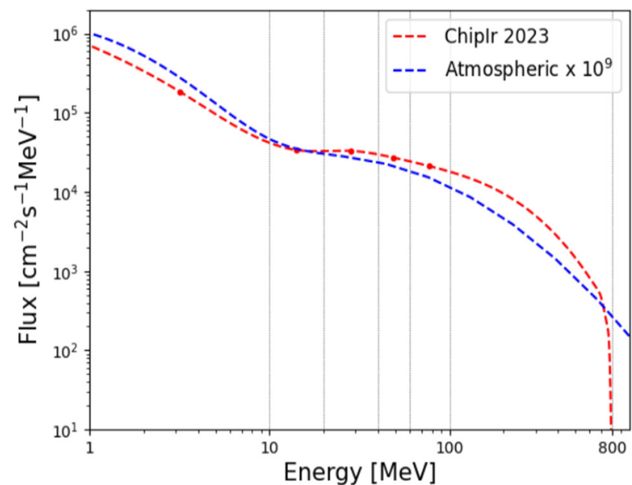

Fig. 2 The ChipIr neutron spectrum (up to 800 MeV) compared to the atmospheric spectrum at Ground level

2 Materials and measurements

SiC power MOSFETs samples were supplied by STMicroelectronics. The packaged samples were irradiated with high-energy atmospheric-like neutrons at the ChipIr beamline, which operates at the ISIS Neutron and Muon Source at the Rutherford Appleton Laboratory, Chilton (UK) [25]. Following irradiation, the package was removed by etching. The resulting un-packaged samples were then analyzed using complementary analytical techniques at the MRF (Medium-Range Facilities) including XRD computed tomography (XCT), profilometry, and scanning electron microscopy of ISIS@MACH ITALIA (IM@IT). The devices tested are discrete commercial third-generation 4 H-SiC power MOSFETs in TO-247 package, manufactured by STMicroelectronics, with $V_{DS} = 1.2$ kV which is the nominal maximum ratings of drain–source voltage. Figure 1 shows a schematic of the MOSFET devices indicating the sample dimensions. As indicated, the thickness of the power MOSFET N-epitaxial layer is 14 μm.

2.1 Neutron irradiation at the ChipIr beamline

The study of the neutron hardness of power MOSFETs is addressed using the ChipIr beamline which allows accelerated neutron tests with atmospheric-like neutron spectrum.

The ChipIr beamline is a dedicated facility for investigating the impact of high-energy atmospheric-like neutrons on microelectronics. ChipIr utilizes neutrons produced via spallation through a high-energy proton beam (800 MeV) striking a tungsten target. The beamline delivers a broad energy spectrum of neutrons (approximately from 1 to 800 MeV), closely reproducing the terrestrial neutron flux environment, as shown in Fig. 2.

Accelerated testing of electronic devices and systems (between 10^6 and 10^8 times) are possible with a measurement of just one hour at the ChipIr neutron beamline being equivalent to exposing microchips to high-energy neutrons over hundreds of years of flying time in an aircraft. In practice by putting the electronic device in the Chipir beamline for say, an hour, one can measure the equivalent of something like hundreds of years in the real environment. From the number of running hours of each experiment one

Table 1 Number of fails under atmospheric neutron exposure for the investigated power MOSFETs at two different V_{DS} values

V_{DS} (V)	Number of fails	Maximum fluence	Operating years at sea level	Operating years at avionics altitude
700	2	1.63E+11	1.43E+06	3.10E+03
950	22	1.87E+10	1.64E+05	3.56E+02

The maximum neutron fluence is converted into the number of years of exposure at sea level and avionic altitude

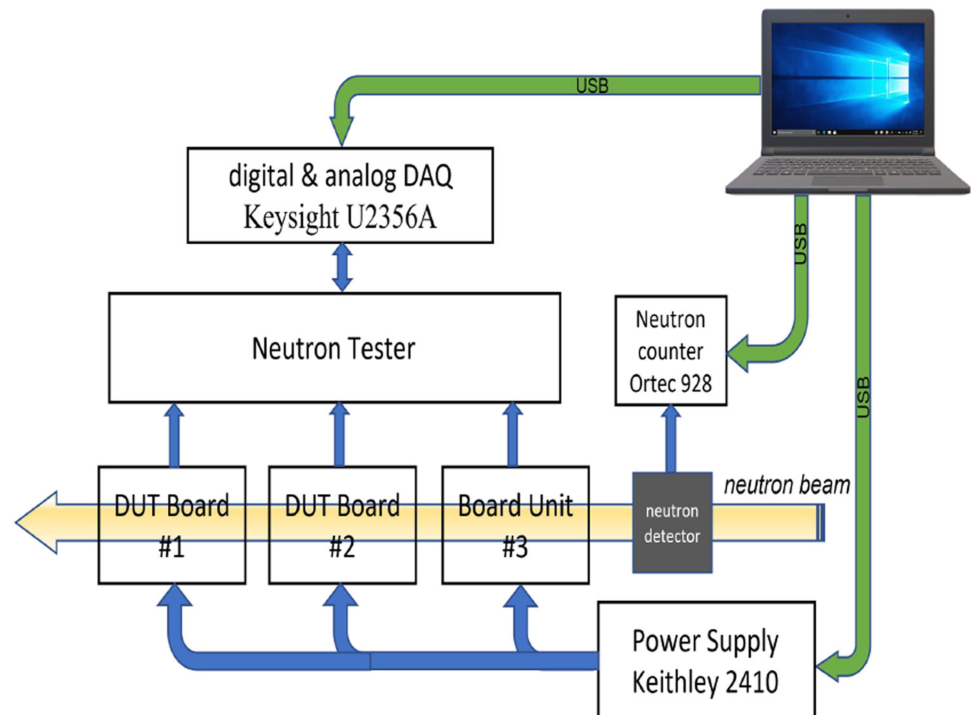

Fig. 3 STMicroelectronics neutron test set-up

can estimate the corresponding years of exposure at sea level and at avionics altitude. Examples are reported in Table 1. In the case of 2 fails (using the criteria: the leakage current of single DUT is higher than 100 μA), the maximum fluence corresponds to about 1 million years at sea level and about thousands of years at airborne altitudes. The FIT values of the neutron failure increase with increasing V_{DS} value [12], hence we choose the irradiation condition at $V_{DS} = 700$ V which is the required operating value for these devices in most applications. The irradiation at $V_{DS} = 950$ V allowed us to increase the number of failed devices. Table 1 shows that the number of failures recorded at $V_{DS} = 700$ V is two, while at $V_{DS} = 950$ V it increases by roughly one order of magnitude. The associated maximum neutron fluence values exhibit the opposite trend, being one order of magnitude higher and lower, respectively. The same difference, one order of magnitude, is observed for both Operating years at sea level and Operating Years at avionics altitude.

The facility is optimized for high-intensity irradiation, allowing accelerated reliability testing of semiconductor devices by providing years' worth of neutron exposure within a short experimental timeframe. The beamline is equipped with a well-characterized neutron flux and spectrum, bench-marked against standard atmospheric neutron environments. The high flux intensity, approximately 5×10^6 n cm^{-2} s^{-1}, enables rapid assessment of SEB and SEE cross sections in electronic components. The collimator configuration defines a neutron minimum beam size of 70×70 mm^2 [21]. The SEB depends on a random burnout that is mainly influenced by the energy of incoming neutrons and the affected area of the device:

- If neutrons hit the sensitive area or near this, a burnout phenomenon can be observed, according to a probability given by the event cross section.
- If neutrons hit an area far from the sensitive one, a small visible impulse is produced and there is not a burnout.

The aim of this test was to produce a few failed SiC devices to perform different failure analysis methodology which could be useful for better failure mechanism comprehension.

In total, 1200 V SiC Power MOSFETs were irradiated with atmospheric neutron in the ChipIr facility in according to the destructive test procedure fixed in Jedec specification JEP151. Figure 3 shows the set-up that was used to perform the neutron test and determine the FIT values of the irradiated devices.

The devices were mounted in three FR4 boards with a total of 24 devices for each irradiation run with biasing condition $V_{GS} = 0$ V and V_{DS} up to 1100 V. It measures the leakage of single DUT and when the device fails (using the criteria: the leakage current is higher than 100 mA) switch off the device's power supply and a digital signal is provided to the LabVIEW software throw the Digital Analog acquisition system to mark the relative SEB failure induced by neutron irradiation, confirming that the lattice temperature reached the sublimation point of SiC. In addition, the system uses the TTL signal available in the neutron facility to count the neutron fluence.

2.2 Measurements of surface and bulk structure of MOSFETs device

After the ChipIr neutron irradiation, the MOSFETs were subjected to a campaign of experiments using complementary analytical techniques. Aims were to derive information of the 2D–3D morphology, structure, and residual strains of the SEBs micro-burning induced by the fast neutron irradiation, using X-Ray computed tomography (XCT) , SEM, and profilometry.

2.3 XRD tomography (XCT)

X-ray computed tomography (XCT) is a non-destructive imaging technique (3D and 2D) that enables the high-resolution reconstruction of a sample's internal structure by analyzing the attenuation of X-rays as they pass through the material. In this study, XCT was used to investigate irradiated SiC power MOSFET devices to reconstruct possible SEB structures, identify internal burnout not visible externally, and compare the structural integrity between "failed" and "non-failed" devices. The following experiments were performed:

1. One "failed" device at maximum neutron fluence (1.63×10^{11} n cm^{-2}).
2. One "non-failed" device.

XCT analyses were performed using a Rigaku Nano3DX system (Rigaku Corporation, Tokyo, Japan), which features parallel-beam geometry and can achieve sub-micrometer spatial resolution. For optimal imaging contrast and penetration through the SiC material, a molybdenum (Mo) anode was selected, operating at 50 kV and 24 mA, providing pseudo-monochromatic X-ray radiation. Each sample was mounted on the nano-manipulator of the instrument, positioned a few mm from a high-resolution CMOS camera with a 20X objective lens, yielding a Field Of View (FOV) of 0.598×0.598 mm^2, a 2048×2048 pixel sensor with a pixel size of 293 nm. To ensure appropriate sampling in accordance with the Nyquist-Shannon theorem, angular projections were acquired in the range [0°, 360°) [27]. The acquisition was performed in a uniformly spaced angular scan, with an exposure time of 15 s per radiograph, and a total of 2027 projections. Ten flat-field and five dark-field images were collected prior to tomography for normalization. The data analysis, including data pre-processing, reconstruction, and quantitative image quality assessments, was performed using the NeuTomPy toolbox software [28], whereas the volume rendering and quantification steps of the samples using Avizo [29] and VGSTUDIO MAX software [30]. Data normalization was conducted through log-transformation, flat-fielding, and dark subtraction, with an additional correction for photon dose [31]. This dose correction ensured that all measured projections received a consistent number of incoming photons, accounting for the stability of the X-ray beam flux. The normalization was applied using the following formula:

$$p = -\log\left(\frac{D_{flat}}{D} \cdot \frac{I - I_{dark}}{I_{flat} - I_{dark}}\right) \tag{1}$$

where I is the raw projection image; I_{dark} and I_{flat} are the mean of the dark-field and flat-field images, respectively, D and D_{flat} are the median computed within a Region Of Interest (ROI) free of sample in the projections and flat images, respectively. The final reconstructed XCT slices of the samples have been achieved by processing the acquired radiographic data set with a "filtered back projection" (FBP) CT reconstruction algorithm available in the NeuTomPy toolbox, followed by a "non-local means" (NLM) post-process denoising filtering step [32, 33]. An image spatial resolution of about 0.6 µm was achieved.

The analysis of the XCT data enables to reconstruct the 3D and 2D of both SiC and SEB structures in the "failed" device. Figure 4 shows the XCT volume rendering of the SiC power MOSFET and the different cross section (xy, xz, and yz) along with four views of the SiC structure and the SEB. The latter has been isolated through segmentation and is displayed in red in the figure. Orthogonal 2D views of the reconstructed volume are presented in panels (d)–(f) of Fig. 4. The analysis of the reconstructed SEB region enabled the determination of the depth at which the SEB originated, as indicated in panel (c), measuring approximately 12.08 µm. The maximum lateral extensions of the SEB in the x and y directions were determined by directly inspecting the various slices and selecting the one where these values were the largest. This analysis yielded measurements of 36.2 and 39.5 µm, respectively.

The SEB volume was determined by counting the number of voxels, a process performed automatically in Avizo after segmenting the defect. By converting this count and using the known voxel size one can estimate the SEB volume. The result of the SEB volume obtained was 9694 µm^3 as reported in Table 2.

A further important finding of the 3D XCT analysis regards the search of volume fractures in the volume of MOSFET devices which could occur after ChipIr neutron irradiation, following the sudden fusion of the materials induced by the Joule effect (precisely the burnout) after the ionization of the materials due to neutron interaction. The 3D rendering shows no volume fractures in the device. The XCT analysis performed on the "non-failed" MOSFET device did not reveal any SEB or defect in the device.

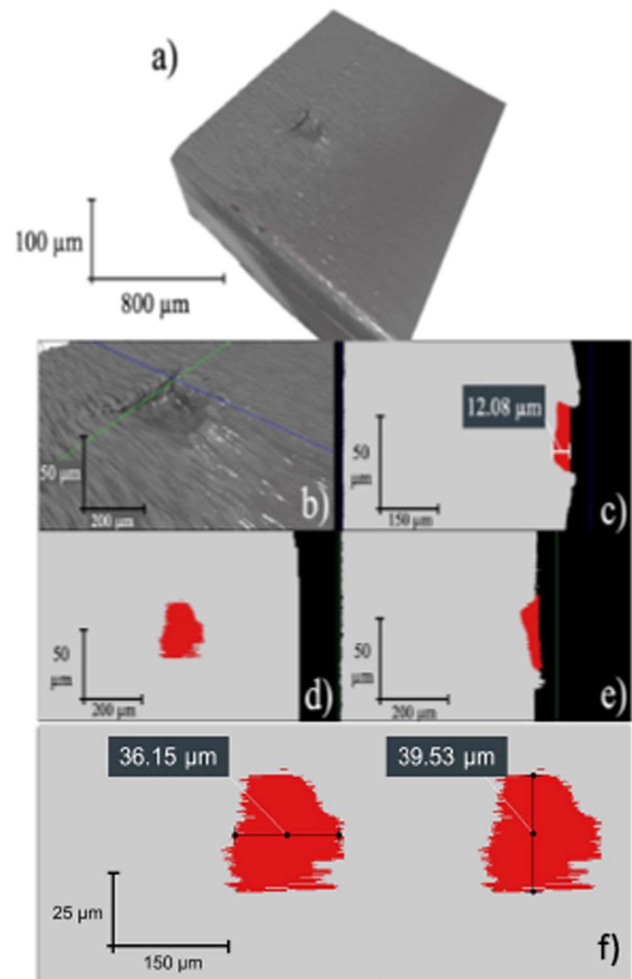

Fig. 4 **a** Device volume reconstruction from XCT; **b** zoom on the SEB defect; **c**–**e** orthogonal 2D views; **f** SEB depth

2.4 Profilometer

A Zeta-20 optical profilometer [34] was used to characterize SEB in the SiC devices. Profilometry is a non-contact 3D imaging and metrology technique that integrates a ZDotTM-based vertical scanning mechanism, along with a wide-area interferometer and a spectroscopic reflectometer. In the ZDotTM mode, the Zeta-20 generates a 3D surface image by capturing a series of images at different heights, typically separated by a few nanometres. Each image is then analyzed to identify the pixels in the sharpest focus, recording their height and colour. Once all pixels have been processed, the system reconstructs a true-colour representation of the surface. Unlike conventional vertical scanning microscopes, the Zeta-20 features a unique optical design that achieves a height resolution of 10 nm, significantly exceeding the typical 700-nm resolution of standard vertical scanning microscopes. For the optical evaluation of the morphology at the micrometric scale, first the device packaging was removed to have better access of the light probe to the SEB. The SiC power MOSFET was then positioned in the sample manipulator of the KLA Zeta-20 instrument and scans were obtained by continuously varying the focal plane of the instrument. The SEB was investigated at different spatial resolution using different lenses. Figure 5 shows the reconstruction of the 3D scans of the SEB.

Figure 6 illustrates the bi-dimensional [panels (a) and (c)] and three-dimensional [panels (b) and (d)] reconstructions which reveal the burnout failure in the SiC MOSFET induced by the ChipIr fast neutron irradiation. The conic-shaped damaged region was caused by the expansion stress that occurred within the device during a SEB. This suggests that the lattice temperature reached the sublimation temperature of SiC, as observed by simulations in a previous study [16]. The polyamide passivation is a standard layer for SiC power devices. It was applied in the component's edge termination region to protect the structure and sustain high voltage.

Furthermore, Joule heating occurred in the n-drift region (14 µm thickness), where an electric field was applied, rapidly driving the temperature to the sublimation threshold due to the high current density induced by the SEB event. The long crack tails in the bottom part of the SEB region in panel (b) further indicate the rapid expansion of the lattice. To better quantify the depth at which the SEB damage penetrated, the line profile shown in panel (c) of Fig. 7 was used. This profile was obtained by intersecting the 2D SEB with a line [panel (a)], which is also shown in the 3D SEB reconstruction for completeness [panel (b)], passing through the burnout region at depth. The line profile shows that the maximum extent of the SEB damage reaches two distinct locations, both

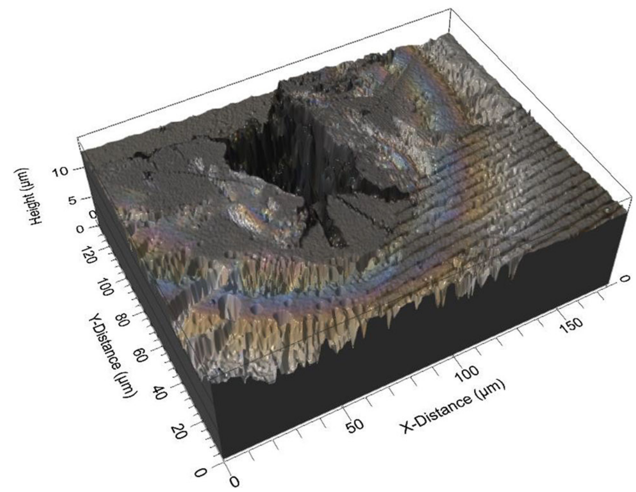

Fig. 5 3D scan of the SEB (induced by fast neutrons) reconstructed by means of light probes

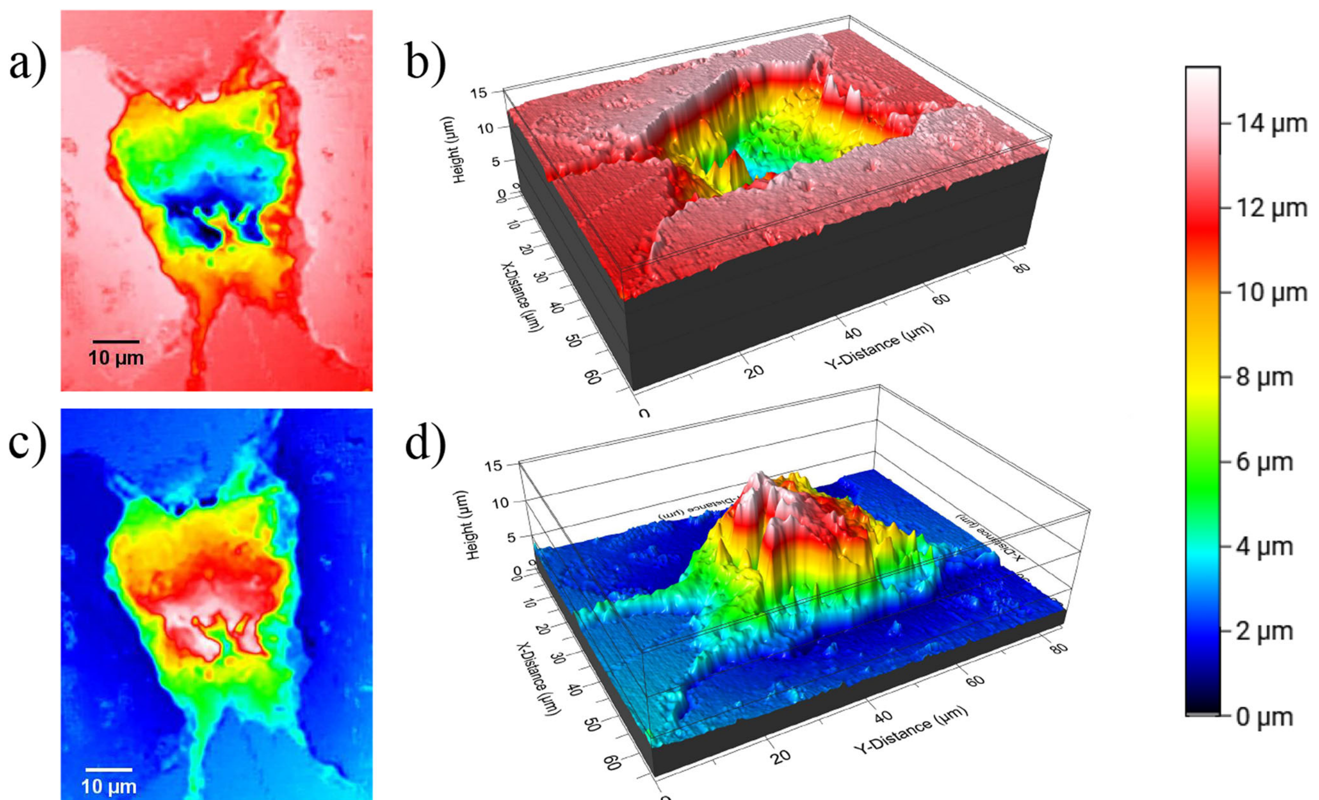

Fig. 6 Profilometer images of the same SEB hole structure shown in Fig. 5, viewed from a different angle. **a** 2D and **b** 3D views show the original shape, plus **c** 2D and **d** 3D views after the mirroring operation that inverted the defect structure

approximately 12 µm deep. This observed damage depth is highly consistent with the known thickness of the active N-drift layer (as illustrated in panel (d)), which strongly suggests that the SEB current filament was sustained through the entire drift region down to the N+ substrate interface. This finding supports simulation results, such as those by Ball et al. [23], which estimate the SEB initiation sensitive volume is near the epitaxial–substrate interface in the case of neutron irradiation. The SEB size was quantified using line profiles taken at the points of maximum extension and fitted with a trapezoidal function, as shown in Fig. 8.

The full width at half maximum (FWHM) obtained from the fit, chosen as a metric for the SEB size, indicates a maximum SEB dimension of 31.2×29.9 µm ($W \times H$), as summarized in Table 2. The 3D SEB reconstruction allowed for the determination of the volumetric extension of the burnout, which was calculated by integrating the plot reported in panel (d) of Fig. 5, after restoring the baseline with a plane fitting the region not interested by the SEB. The calculated volume value corresponds to 9600 µm^3. Figure 8 shows the line profiles carried out for the quantitative evaluation of the linear extension of the defect in the two horizontal and vertical spatial directions. Figure 9 shows the panel (e) of Fig. 8 magnified.

Fig. 7 View of the mirrored defect, where a plane intersects the highest roughness points of the bump. **a** 2D image of the SEB. The red line represents the points where the profile was traced. **b** 3D view where the traced plane is highlighted. **c** Line profile of the roughness points corresponding to the traced plane

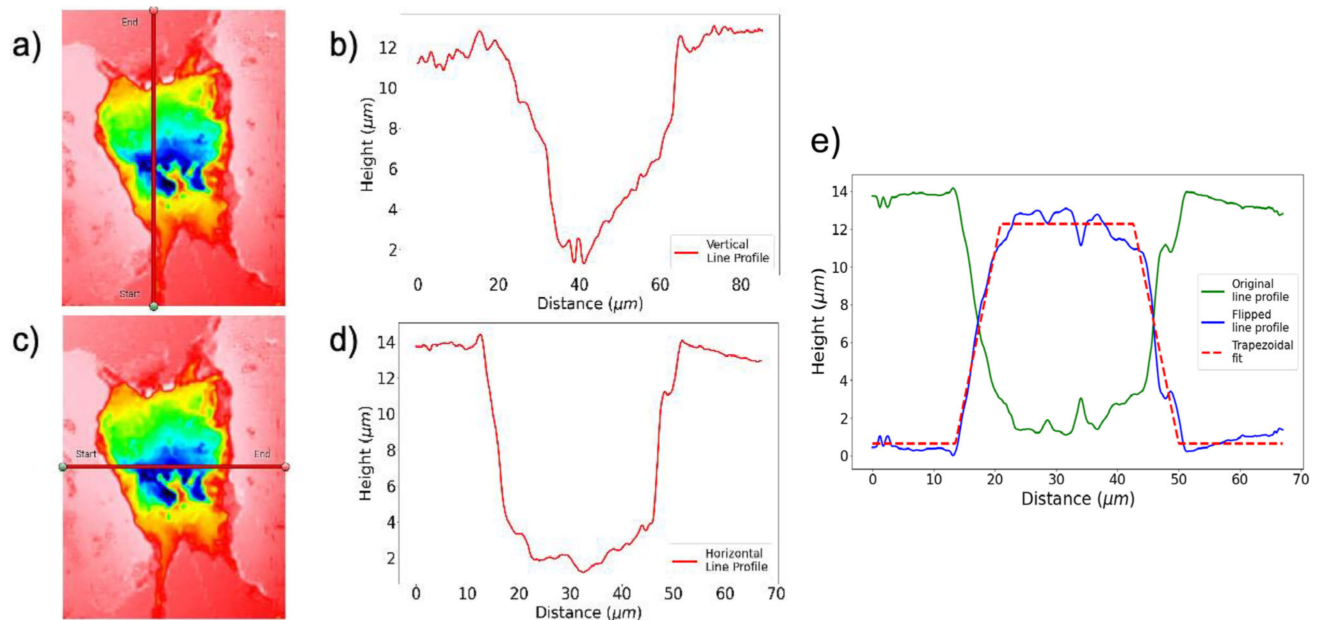

Fig. 8 2D image of the SEB crack from which the vertical **a** and horizontal **c** line profiles and the respective one-dimensional plots of the vertical (**b**) and horizontal (**d**) trends were extracted. Line profile of the SEB crack: the original data are shown in green, the inverted line profile in blue and fit with trapezoidal function in red (**e**)

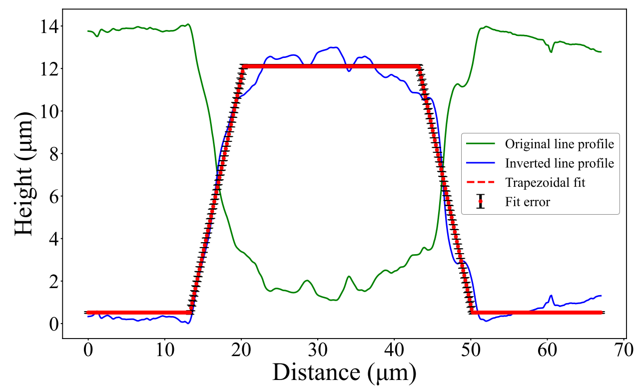

Fig. 9 Line profile of the SEB, the original data are shown in green, the inverted line profile in blue and fit with trapezoidal function in red

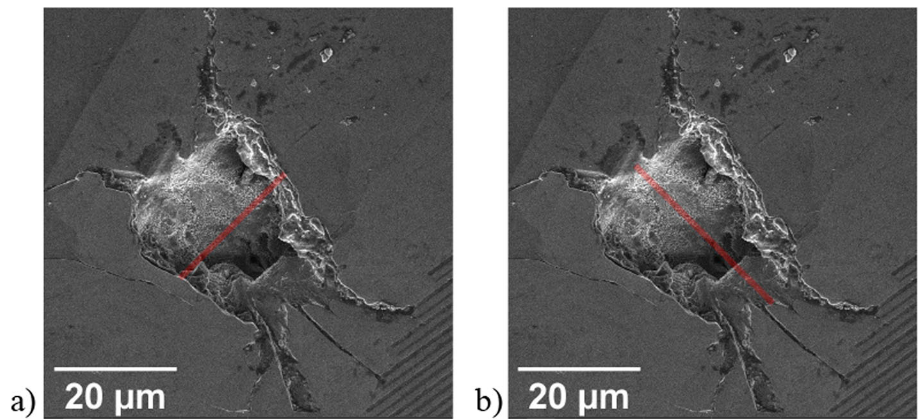

Fig. 10 The SEM micrographs of the one-dimensional SEB profile. The measured size of the SEB is highlighted in red: approximately **a** 24 μm for the horizontal and **b** 32 μm for the vertical dimension

Table 2 Results of the SEB dimensions obtained from the three experimental techniques used

Technique	X dimension (μm)	Y dimension (μm)	Z dimension (μm)	Volume (μm^3)	
Profilometer	31.20 ± 0.08	29.90 ± 0.23	11.50 ± 0.06	$9600 \pm 1.0 \times 10^{-6}$	
	SEM	24.30 ± 0.10	32.20 ± 0.10	–	–
	XCT	$36.2 \pm 3.5 \times 10^{-4}$	$39.5 \pm 3.5 \times 10^{-4}$	$12.1 \pm 3.5 \times 10^{-4}$	$9694 \pm 4.3 \times 10^{-1}$

2.5 Scanning electron microscopy

The SEB extension was measured by scanning electron microscopy (SEM), using a TESCAN VEGA (4th series) electron microscope. SEM is a surface-sensitive technique that reconstructs the topography of a sample by detecting secondary electrons generated from the interaction between a high-energy electron beam and the surface of a specimen. The instrument is equipped with an extra-large analytical chamber and multiple detectors, including an Everhart-Thornley secondary electron (SE) detector, a back-scattered electron (BSE) detector, and an X-ray detector for energy dispersive spectroscopy (EDS) microanalysis. Secondary electron images were acquired under high-vacuum conditions (10^{-5} mbar) using a beam energy of 5 kV and a beam current of 10 pA, selected as the optimal trade-off between electron penetration and spatial resolution.

To analyze the morphology and dimensions of SEB, the surfaces of MOSFET devices were examined from a top-view perspective at a magnification of 2.6 Kx. The SEM images provided a detailed two-dimensional visualization of the SEB structures, and the high magnification revealed their depth spatial extent. Measurements were performed using ImageJ software with line tools, following prior image calibration based on magnification. Figure 10a reports the quantification of the SEB extension in the horizontal direction (also indicated in Table 2 with x-axis) of about 24.3 μm and of the vertical one of 32.2 μm (also indicated in Table 2 with y-axis). The results of the SEM measurements are in good agreement with those obtained by optical profilometry (see Table 2 and Fig. 11).

In addition, the images reveal cracks that extend from the SEB edge, reflecting the crystalline structure of SiC. These cracks were also observed in the profilometry data of Figs. 7 and 11. In this case as well, the damage exhibits axisymmetric around the central void, due to the highly localized SEB current. The volumetric evaluation of the SEB performed with XCT and optical profilometry data are all in very good agreement. In both cases, a defect volume of approximately 9600 μm^3 was recorded (see Table 2 and Fig. 11).

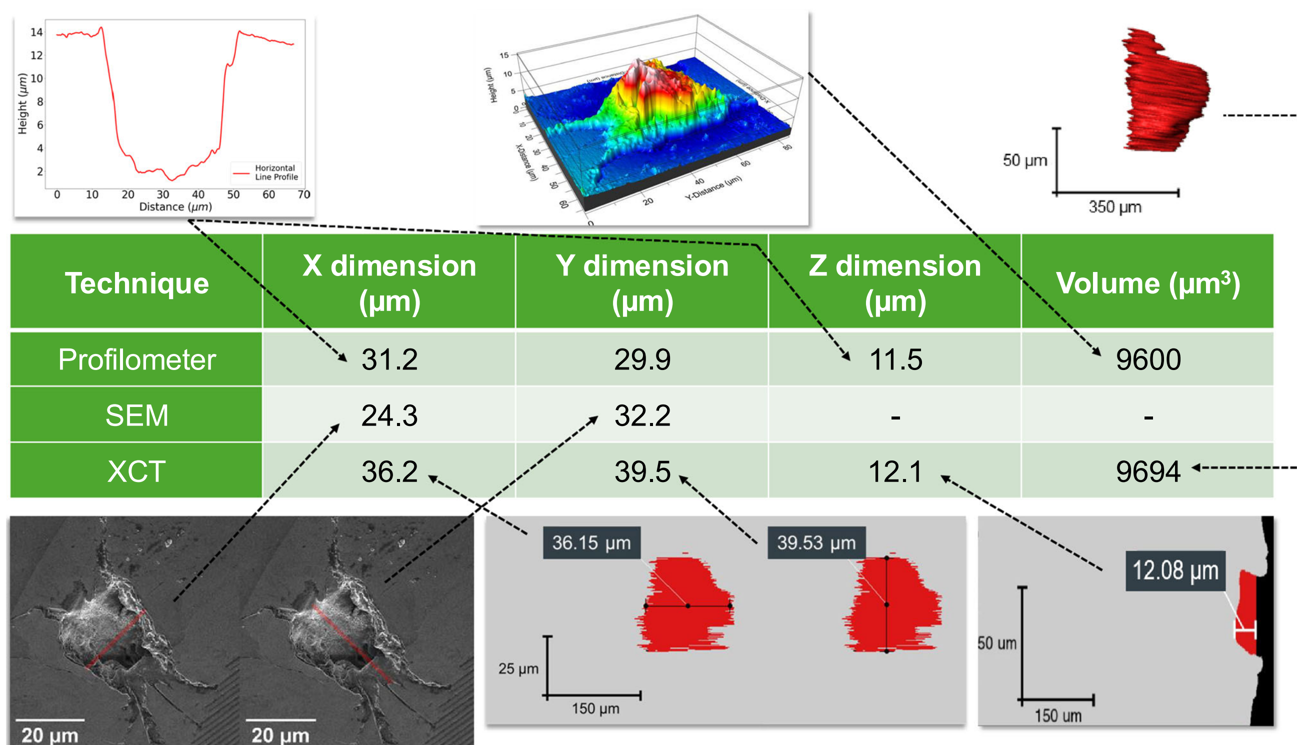

Fig. 11 Results for SEB size from the three analytical instruments

3 Results and conclusions

These studies present complementary characterizations of packaged MOSFETs irradiated with accelerated neutrons at the ChipIr beamline of the ISIS facility, and after unpackaging by etching, were analyzed using electron and photon probes with advanced instrumentation at the IM@IT facility. The experimental results confirm that neutron irradiation induces a single, localized SEB in the packaged MOSFETs, suggesting that the lattice temperature reached the sublimation point of SiC.

The combined results obtained from the different analytical techniques provide a complete 2D and 3D morphology of the single SEB induced by ChipIr neutron irradiation in the SiC power MOSFETs. The single burnout was observed without cumulative effects. A key outcome of this study is the excellent agreement among the measurements obtained from the three independent techniques, i.e. XCT, profilometry, and SEM. In particular, the 3D SEB volume data are highly consistent. The 3D reconstructions derived from XCT and profilometry show a similar spatial extent of the SEB, with a burnout volume of approximately 9600 μm^3 and a depth of about 12 μm in the 14 μm thick MOSFET (Table 2 and Fig. 11). A statistical analysis of the distribution of SEB dimensions and volumes from a large number of SiC power MOSFETs damaged by atmospheric neutrons (tested under different bias voltages) is currently in progress. Such studies aim to provide valuable insight into the mechanism of SEB formation, its electric-field configuration, and its evolution as a function of the applied voltage, thereby underscoring the importance of radiation-hardening strategies to enhance the resilience of SiC-based power electronics in critical applications such as aerospace, nuclear energy, and high-reliability power systems.

Acknowledgements The authors gratefully acknowledge the support of the ISIS@MACH ITALIA Research Infrastructure, the hub of ISIS Neutron and Muon Source (UK), [MUR official registry U. 0008642.28-05-2020—16th April 2020], listed in the Italian Ministry of University and Research's Piano Nazionale delle Infrastrutture di Ricerca (PNIR 2021-2027) "in the broader notion of ISIS". The financial support from the Consiglio Nazionale delle Ricerche within the CNR-STFC Grant Agreement [No. 2021-2027] concerning collaboration in scientific research at the ISIS (UK) of STFC, is gratefully acknowledged. ISIS Facility and IM@IT are jointly listed in high priority RI's (see Table 6, p. 30, note 38, PNIR in 2021-2027). CA, SL and TM acknowledge the financial support of the Italian Ministry of defence within the project HI-CHIPS "Radiation hardness tests of hard Si/SiC/GaAs/GaN based chips and chip components of pacing-based devices for ICT applications" (2024–2025) and Ms Cadia D'Ottavi for her valuable technical support.

Funding Open access funding provided by Università degli Studi di Roma Tor Vergata within the CRUI-CARE Agreement.

Data Availability The datasets generated and analyzed during the current study are available from the corresponding author on reasonable request.

Open Access This article is licensed under a Creative Commons Attribution 4.0 International License, which permits use, sharing, adaptation, distribution and reproduction in any medium or format, as long as you give appropriate credit to the original author(s) and the source, provide a link to the Creative Commons licence, and indicate if changes were made. The images or other third party material in this article are included in the article's Creative Commons licence, unless indicated otherwise in a credit line to the material. If material is not included in the article's Creative Commons licence and your intended

use is not permitted by statutory regulation or exceeds the permitted use, you will need to obtain permission directly from the copyright holder. To view a copy of this licence, visit http://creativecommons.org/licenses/by/4.0/.

References

1. P.K. Grieder, *Extensive Air Showers: High Energy Phenomena and Astrophysical Aspects—A Tutorial, Reference Manual and Data Book* (Springer, Berlin, Heidelberg, 2010). https://doi.org/10.1007/978-3-540-76941-5
2. L. Desorgher, E. Flückiger, M. Gurtner, M. Moser, R. Bütikofer, Atmocosmics: a geant 4 code for computing the interaction of cosmic rays with the earth's atmosphere. Int. J. Mod. Phys. A **20**(29), 6802–6804 (2005). https://doi.org/10.1142/S0217751X05030132
3. T.K. Gaisser, R. Engel, E. Resconi, *Cosmic Rays and Particle Physics* (Cambridge University Press, Cambridge, 2016)
4. M. Cecchetto, R. García Alía, F. Wrobel, Impact of energy dependence on ground level and avionic see rate prediction when applying standard test procedures. Aerospace (2019). https://doi.org/10.3390/aerospace6110119
5. *Process Management for Avionics-Atmospheric Radiation Effects. Guidelines for Single Event Effects Testing for Avionics Systems, Iec Standard 62396-2* (Technical report, International Electrotechnical Commission, Geneva, 2017)
6. M. Shea, D. Smart, Cosmic ray implications for human health. Space Sci. Rev. **93**, 187–205 (2000). https://doi.org/10.1023/A:1026544528473
7. G. Soelkner, Ensuring the reliability of power electronic devices with regard to terrestrial cosmic radiation. Microelectron. Reliab. **58**, 39–50 (2016). https://doi.org/10.1016/j.microrel.2015.12.019
8. J.F. Ziegler, Terrestrial cosmic rays. IBM J. Res. Dev. **40**(1), 19–39 (1996). https://doi.org/10.1147/rd.401.0019
9. E. Petersen, *Single Event Effects in Aerospace* (Wiley, 2011). https://doi.org/10.1002/9781118084328
10. R. Velazco, D. McMorrow, J. Estela,*Radiation Effects on Integrated Circuits and Systems for Space Applications* (Springer, 2019). https://doi.org/10.1007/978-3-030-04660-6
11. H. Quinn, The use of accelerated radiation testing for avionics, in *AIP Conference Proceedings*, vol. 1525 (American Institute of Physics, 2013), pp. 643–648. https://doi.org/10.1063/1.4802406
12. F. Principato, S. Altieri, L. Abbene, F. Pintacuda, Accelerated tests on si and sic power transistors with thermal, fastand ultra-fast neutrons. Sensors **20**(11), 3021 (2020). https://doi.org/10.3390/s20113021
13. A.F. Witulski, D.R. Ball, K.F. Galloway, A. Javanainen, J.-M. Lauenstein, A.L. Sternberg, R.D. Schrimpf, Single-event burnout mechanisms in sic power mosfets. IEEE Trans. Nucl. Sci. **65**(8), 1951–1955 (2018). https://doi.org/10.1109/TNS.2018.2849405
14. K. Niskanen, R. Coq Germanicus, A. Michez, F. Wrobel, J. Boch, F. Saigné, A.D. Touboul, Neutron-induced failure dependence on reverse gate voltage for sic power mosfets in atmospheric environment. IEEE Trans. Nucl. Sci. **68**(8), 1623–1632 (2021). https://doi.org/10.1109/TNS.2021.3077733
15. R.C. Germanicus, K. Niskanen, A. Michez, N. Moultif, W. Jouha, O. Latry, J. Boch, U. Lüders, A.D. Touboul, Failure analysis of atmospheric neutron-induced single event burnout of a commercial sic mosfet. Mater. Sci. Forum **1062**, 544–548 (2022). https://doi.org/10.4028/p-973n9u
16. R. Coq Germanicus, A. Michez, K. Niskanen, M. Chaudhary, G. Bascoul, V. Chazal, F. Wrobel, J. Boch, Single event effects of sic power mosfets: from neutron interaction to destruction at the die level. IEEE Trans. Nucl. Sci. **72**(8), 2368–2376 (2025). https://doi.org/10.1109/TNS.2025.3561583
17. C. Martinella, P. Natzke, R.G. Alia, Y. Kadi, K. Niskanen, M. Rossi, J. Jaatinen, H. Kettunen, A. Tsibizov, U. Grossner, A. Javanainen, Heavy-ion induced single event effects and latent damages in sic power mosfets. Microelectron. Reliab. **128**, 114423 (2022). https://doi.org/10.1016/j.microrel.2021.114423
18. M. Buffolo, D. Favero, A. Marcuzzi, C. De Santi, G. Meneghesso, E. Zanoni, M. Meneghini, Review and outlook on gan and sic power devices: Industrial state-of-the-art, applications, and perspectives. IEEE Trans. Electron Devices **71**(3), 1344–1355 (2024). https://doi.org/10.1109/TED.2023.3346369
19. A. Marcuzzi, Favero, D., Santi, C.D., Meneghesso, G., Zanoni, E., Meneghini, M.: A review of sic commercial devices for automotive: properties and challenges, in *2023 AEIT International Conference on Electrical and Electronic Technologies for Automotive (AEIT AUTOMOTIVE)* (2023), pp. 1–6. https://doi.org/10.23919/AEITAUTOMOTIVE58986.2023.10217233
20. A. Akturk, R. Wilkins, J. McGarrity, Terrestrial neutron induced failures in commercial sic power mosfets at 27c and 150c, in *2015 IEEE Radiation Effects Data Workshop (REDW)* (2015), pp. 1–5. https://doi.org/10.1109/REDW.2015.7336737
21. A. Hands, P. Morris, K. Ryden, C. Dyer, P. Truscott, A. Chugg, S. Parker, Single event effects in power mosfets due to atmospheric and thermal neutrons. IEEE Trans. Nucl. Sci. **58**(6), 2687–2694 (2011). https://doi.org/10.1109/TNS.2011.2168540
22. J.L. Titus, An updated perspective of single event gate rupture and single event burnout in power mosfets. IEEE Trans. Nucl. Sci. **60**(3), 1912–1928 (2013). https://doi.org/10.1109/TNS.2013.2252194
23. D.R. Ball, B.D. Sierawski, K.F. Galloway, R.A. Johnson, M.L. Alles, A.L. Sternberg, A.F. Witulski, R.A. Reed, R.D. Schrimpf, A. Javanainen, J.-M. Lauenstein, Estimating terrestrial neutron-induced seb cross sections and fit rates for high-voltage sic power mosfets. IEEE Trans. Nucl. Sci. **66**(1), 337–343 (2019). https://doi.org/10.1109/TNS.2018.2885734
24. C. Andreani, A. Pietropaolo, A. Salsano, G. Gorini, M. Tardocchi, A. Paccagnella, S. Gerardin, C.D. Frost, S. Ansell, S.P. Platt, Facility for fast neutron irradiation tests of electronics at the isis spallation neutron source. Appl. Phys. Lett. **92**(11), 114101 (2008). https://doi.org/10.1063/1.2897309
25. C. Cazzaniga, N. Bhuiyan, M. Kastriotou, D. Chiesa, S. Lilley, C.D. Frost, Fast neutron measurements for the characterization of the chipir beamline. IEEE Trans. Nucl. Sci. (2024). https://doi.org/10.1109/TNS.2024.3416540
26. T. Shoji, S. Nishida, K. Hamada, H. Tadano, Analysis of neutron-induced single-event burnout in sic power mosfets. Microelectron. Reliab. **55**(9–10), 1517–1521 (2015)
27. A.C. Kak, M. Slaney, G. Wang, Principles of computerized tomographic imaging. Med. Phys. **29**(1), 107–107 (2002). https://doi.org/10.1118/1.1455742
28. D. Micieli, T. Minniti, G. Gorini, Neutompy toolbox, a python package for tomographic data processing and reconstruction. SoftwareX **9**, 260–264 (2019). https://doi.org/10.1016/j.softx.2019.01.005
29. Avizo Software, Thermo Fisher Scientific Website. https://www.thermofisher.com/uk/en/home/industrial/electron-microscopy/electron-microscopy-instruments-workflow-solutions/3d-visualization-analysis-software.html
30. VGSTUDIO MAX Software, Hexagon Website. https://volumegraphics.hexagon.com/en/products/vgstudio-max.html
31. D. Micieli, T. Minniti, V. Formoso, W. Kockelmann, G. Gorini, A comparative study of reconstruction methods applied to neutron tomography. J. Instrum. **13**(06), 06006–06006 (2018). https://doi.org/10.1088/1748-0221/13/06/c06006
32. T. Minniti, F. Schoofs, L.M. Evans, W. Kockelmann, J.-H. You, H. Lewtas, Structural integrity of demo divertor target assessed by neutron tomography. Fusion Eng. Des. **169**, 112661 (2021). https://doi.org/10.1016/j.fusengdes.2021.112661
33. D. Micieli, T. Minniti, L.M. Evans, G. Gorini, Accelerating neutron tomography experiments through artificial neural network based reconstruction. Sci. Rep. **9**(1), 2450 (2019). https://doi.org/10.1038/s41598-019-38903-1
34. KLA Website. https://www.kla.com/products/instruments/optical-profilers/zeta-20#details.html